RESEARCH ARTICLE

Meander of a fin trailing vortex and the origin of its turbulence

Steven J. Beresh · John F. Henfling ·
Russell W. Spillers

Abstract The low-frequency meander of a trailing vortex shed from a tapered fin installed on a wind tunnel wall has been studied using stereoscopic particle image velocimetry in the near-wake at Mach 0.8. Distributions of the instantaneous vortex position reveal that the meander amplitude increases with downstream distance and decreases with vortex strength, indicating meander is induced external to the vortex. Trends with downstream distance suggest meander begins on the fin surface, prior to vortex shedding. Mean vortex properties are unaltered when considered in the meandering reference frame, apparently because turbulent fluctuations in the vortex shape and strength dominate positional variations. Conversely, a large peak of artificial turbulent kinetic energy is found centered in the vortex core, which almost entirely disappears when corrected for meander, though some turbulence remains near the core radius. Turbulence originating at the wind tunnel wall was shown to contribute to vortex meander by energizing the incoming boundary layer using low-profile vortex generators and observing a substantial increase in the meander amplitude, while greater turbulent kinetic energy penetrates the vortex core. An explanatory mechanism has been hypothesized, in which the vortex initially forms at the apex of the swept leading edge of the fin where it is exposed to turbulent fluctuations within the wind tunnel wall boundary layer, introducing an instability into the incipient vortex core.

S. J. Beresh (✉) · J. F. Henfling · R. W. Spillers
Sandia National Laboratories, PO Box 5800,
Mailstop 0825, Albuquerque, NM 87185, USA
e-mail: sjberes@sandia.gov

1 Introduction

Any finite lifting surface at angle of attack inescapably generates a trailing vortex that rolls up from the tip owing to the pressure difference between the windward and leeward surfaces. These trailing vortices are quite strong and dominate the wake, typically persisting for a great distance downstream. As a result of their broad importance to flight hardware and their embodiment of fundamental fluid dynamics, trailing vortices have been studied extensively in wind tunnels, tow tanks, and in flight.

It has been well established by past investigations that trailing vortices exhibit a low-frequency meander (alternatively termed "wander") in wind tunnels, in which a random lateral drift of the vortex core about a mean point is observed at frequencies much lower than those associated with turbulent motion (Corsiglia et al. 1973; Baker et al. 1974; Green and Acosta 1991; Shekarriz et al. 1993; Devenport et al. 1996; Yeung and Lee 1999; Rokhsaz et al. 2000; Jacquin et al. 2001; Heyes et al. 2004; Bailey et al. 2006; Bailey and Tavoularis 2008). This phenomenon typically is attributed to wind tunnel freestream turbulence and therefore is considered an experimental artifact not found in flight conditions (Corsiglia et al. 1973; Baker et al. 1974; Devenport et al. 1996; Bailey et al. 2006; Bailey and Tavoularis 2008). Conversely, Rokhsaz et al. (2000) present data suggesting a cause other than freestream turbulence, and Jacquin et al. (2001) find that meander arises from turbulent fluctuations originating not in the freestream, but rather, in the shear layer as the vortex rolls up from the wing. Heyes et al. (2004) are unable to conclude whether freestream turbulence or shear layer turbulence is responsible for vortex meander, or possibly a combination thereof. A similar meander is observed for the leading-edge vortices on delta wings

even prior to vortex breakdown (Menke and Gursul 1997; Gordnier and Visbal 2005).

Regardless of the source, vortex meander clearly does influence the mean measured properties of the vortex (Corsiglia et al. 1973; Baker et al. 1974; Devenport et al. 1996; Heyes et al. 2004; Bailey et al. 2006; Bailey and Tavoularis 2008). Devenport et al. (1996) note that meander creates a smoothing effect that can make the vortex appear closer to the classically predicted structure, causing the vortex core to appear to have a larger diameter and reduced peak tangential and axial velocities, consistent with Baker et al.'s (1974) pioneering observations; Heyes et al. (2004) and Bailey and Tavoularis (2008) draw similar conclusions. The same effects were found by Westphal and Mehta (1989) when forcing a low-frequency oscillation on a vortex generator. Artificially large values of turbulent stresses also may result from experiments that do not correct for vortex meander (Devenport et al. 1996; Heyes et al. 2004; Bailey and Tavoularis 2008).

A considerable body of flowfield data has been acquired of trailing vortices generated by lifting surfaces and is readily available in the open literature, but the preponderance of it concerns aircraft wings rather than the low-aspect-ratio control surfaces common to munitions. To provide data tailored toward the control surfaces integral to fin–wake interactions, a recent experiment conducted by the present authors explored the mean properties of the trailing vortex generated by a fin representative of those found on modern precision-guided air-delivered weapons (Beresh et al. 2009a). Stereoscopic particle image velocimetry (PIV) measurements were acquired in the crossplane within the near-field of the flow. Among the findings in this work is that the proximity of the vehicle body influences the behavior of the vortex. The rotational motion of the vortex is seen to draw low-speed turbulent fluid from the wall boundary layer toward the vortex core, which appears to hasten the decay of the vortex and produce a larger axial velocity deficit than might be expected.

Although freestream turbulence probably is a source of vortex meander in the Beresh et al. (2009a) experiment, it may not operate alone. The rollup of the vortex from the low-aspect-ratio fin ingests turbulence from the wall boundary layer, and it would be consistent with the findings of Jacquin et al. (2001) and Heyes et al. (2004) to suppose that this boundary layer turbulence drawn toward the vortex would contribute to meander. If so, this observation would infer that vortex meander may be a phenomenon present in flight for missile geometries, not merely isolated to wind tunnel studies.

The present paper seeks to re-examine the data from Beresh et al. (2009a) with a concentration upon vortex meander. The full-field instantaneous measurements collected using PIV allow a more direct examination of this phenomenon than has been possible for the bulk of the previous studies (notably excepting Heyes et al. 2004), which employed time-sequenced point measurements such as multi-hole Pitot probes or hot-wire anemometry. In particular, the renewed analysis will address whether turbulence from the nearby wall boundary layer bears a responsibility for vortex meander, a potential influence unremarked by prior experiments.

2 Experimental approach

2.1 Experimental hardware

Experiments were performed in Sandia's Trisonic Wind Tunnel (TWT), which is a blowdown-to-atmosphere facility using air as the test gas through a 305×305 mm^2 rectangular test section enclosed within a pressurized plenum. A solid-wall transonic test section was used for the present work rather than the traditional ventilated version because it offers reasonable optical access, a flat plate upon which models may be mounted from the wall, and computationally tractable boundary conditions for comparison of experimental data and numerical simulations.

The fin employed in the present study is drawn in Fig. 1, designed as a generic representation of the various fin geometries that could be found on real-world systems. Based upon a trapezoidal planform, the leading edge sweep is 45°, the fin root chord 76.2 mm, the fin span 38.1 mm, and its thickness 3.18 mm. The sharp leading edge has a taper that terminates at a length of 1/3 the chord. The fin passes through the test section wall and attaches to a rotary mount that can be set to highly repeatable discrete angles of attack ranging from −5° to +10° in 1° increments, ±0.1°, with a center of rotation at the midpoint of the fin root. A gap of 1.5 mm exists between the root of the fin and the wind tunnel wall. The axial position of the fin is adjustable within a range of 457 mm using a series of
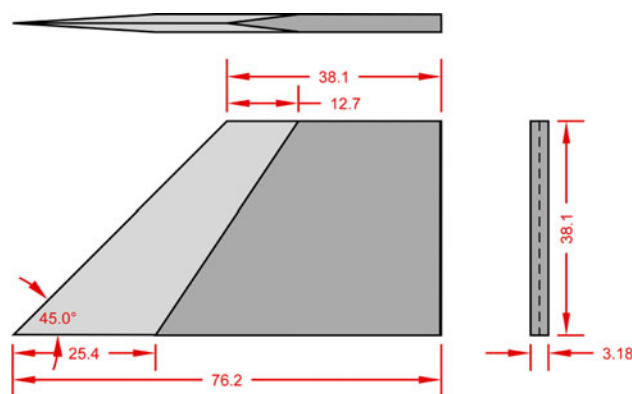

Fig. 1 Sketch of the fin geometry. Dimensions in mm

interchangeable sliding mounting blocks within a rail cut into the test section wall.

2.2 Particle image velocimetry system

The PIV laser sheet configuration for the fin vortex measurements in the TWT is shown in Fig. 2, in which stereoscopic PIV is used to obtain all three velocity components in the wind tunnel crossplane. The laser sheet was aligned normal to the wind tunnel axis and positioned to the midpoint of the test section side-wall window. The limited optical access prevents meaningful movement of the crossplane location upstream or downstream; thus, all data have been acquired at a single position within the test section. Different stations with respect to the fin were achieved by moving the fin's location. The coordinate system is chosen such that the u component lies in the streamwise direction and the v component is in the vertical direction, positive away from the top wall; the w component is chosen for a right-handed coordinate system. The origin is located at the trailing edge of the fin root in its zero angle-of-attack position, regardless of its position along the test section axis.

The light source was a frequency-doubled dual-cavity Nd:YAG laser (Spectra Physics PIV-400) that produced about 400 mJ per beam. The beams were formed into coplanar sheets and directed into the test section from beneath the wind tunnel. To limit the particle dropout arising from the alignment of the freestream direction of the wind tunnel with the out-of-plane motion through the laser sheet, a relatively thick laser sheet of about 2 mm and brief time between pulses of 1.40 μs were employed. Data were collected at 5 Hz, and therefore individual samples are temporally uncorrelated.

The TWT is seeded by a thermal smoke generator (Corona Vi-Count 5000) that produces particles typically 0.2–0.3 μm in diameter from a mineral oil base. Particles are delivered to the TWT's stagnation chamber upstream of the flow conditioning section; a posteriori analysis of the data presented subsequently derives a Stokes number on the order of 0.01, which indicates the particles are sufficiently small that they rapidly attain the local velocity and avoid particle lag biases even in the presence of velocity gradients due to the fin tip vortex (Samimy and Lele 1991; Melling 1997). Particle ejection from the vortex core was not found to be a problem.

Scattered laser light was collected by interline-transfer CCD cameras (Redlake MegaPlus ES4.0/E) with a resolution of 2048 × 2048 pixels. The two cameras were equipped with 200-mm lenses mounted on Scheimpflug platforms to create an oblique focal plane aligned with the laser sheet. Both cameras looked through the same test section window, viewing the laser sheet from opposite directions, because placing one camera at the other side-wall window would have precluded access to the test section. Stereoscopic camera calibrations used the multiplane procedure described by Soloff et al. (1997).

Data were interrogated using LaVision's DaVis v7.1 for greater precision at the expense of spatial resolution using a 64 × 64 pixel window employing a two-pass adaptive correlation to account for the mean streamwise particle displacement. A 50% overlap in the interrogation windows was used as well to oversample the velocity fields. The software incorporates image deformation based upon local velocity gradients, using a bilinear interpolation scheme to warp the images. The resulting vector fields were validated based upon signal-to-noise ratio, nearest-neighbor comparisons, and allowable velocity range.

2.3 Flow conditions

The nominal freestream Mach number is $M_\infty = 0.8$ for all cases shown, with the wind tunnel stagnation pressure $P_0 = 154$ kPa to yield a test section static pressure

Fig. 2 Schematic of the PIV crossplane configuration, looking in the downstream direction from below the test section. Flow is from *right* to *left*. All dimensions are in millimeters. Not to scale
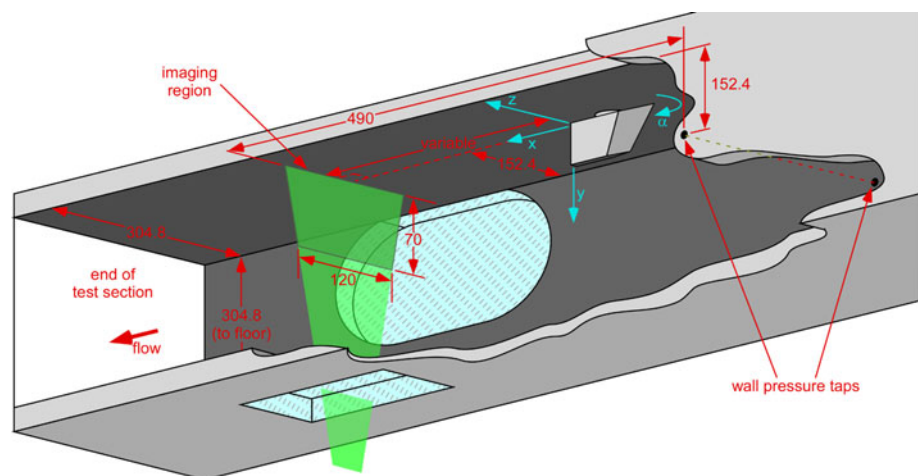
$p_w = 101$ kPa. The freestream stagnation temperature T_0 is subject to minor variation from 316 to 328 K. Freestream turbulence levels are bounded as, at most, 0.5%. The wall pressure p_w was measured from the mean of two static pressure taps located on the wind tunnel side walls 490 mm upstream of the laser sheet location, as seen in Fig. 2. M_∞ was calculated isentropically from the ratio p_w/P_0 and T_0. The freestream Mach number rises with downstream distance due to boundary layer growth on the wind tunnel walls in the constant-area cross-section; hence, the actual Mach number at the measurement position is greater than the nominal value. To determine the local value, a series of pressure taps in one side wall of the test section were recorded during every wind tunnel run, which finds that for a nominal Mach 0.8, an increase to Mach 0.834 is observed at the laser sheet position.

The 99% velocity boundary layer thickness has been measured as 15.4 ± 0.4 mm from PIV data acquired in the streamwise plane (Beresh et al. 2005). This measurement was taken on the wind tunnel centerline at the same downstream position as the crossplane laser sheet.

3 Results

3.1 Velocity fields

Mean velocity data are shown in Fig. 3 at fin angle of attack $\alpha = 10°$, calculated from 2,400 individual realizations acquired over 16 wind tunnel runs; data at additional
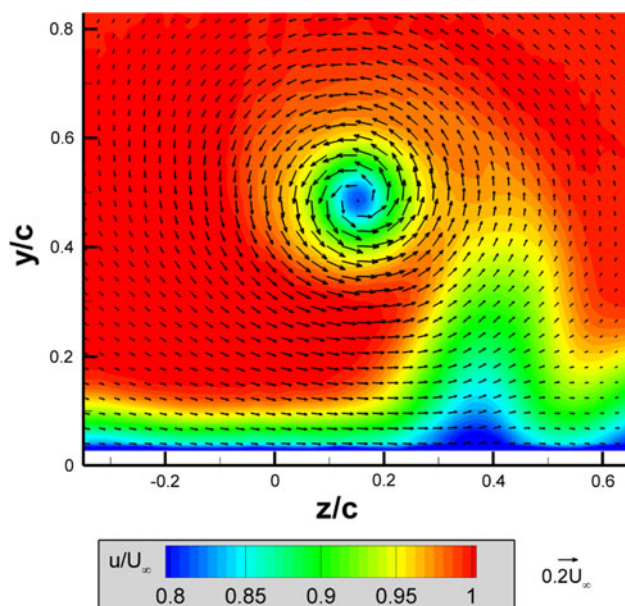

Fig. 3 Mean velocity fields at a distance of $x/c = 4.18$ from the trailing edge of the fin for $\alpha = 10°$. Vectors are subsampled by a factor of two in each dimension

angles of attack are found in Beresh et al. (2009a). The fin was mounted as far upstream in the wind tunnel as possible, thereby placing the PIV measurement location at a distance of $x/c = 4.18$ from the trailing edge of the fin where c is the fin root chord. In-plane velocities are displayed as vectors superposed upon a contour plot of the out-of-plane (streamwise) velocities, with the vectors subsampled by a factor of two in each direction for visual clarity. The axes have been normalized by c and velocities by U_∞ as determined by the PIV data.

Figure 3 shows that the fin tip vortex is clearly visualized, by both the in-plane rotation and the out-of-plane streamwise velocity deficit. The fin tip vortex itself is entirely analogous to the well-known aircraft wing tip vortices. The same characteristic structure is observed here, including the presence of a primary vortex core with a thin vortex sheet continuing to spiral around the core (in the present case, additionally lifting the wall boundary layer) and the prominence of wake-like axial flow within the vortex core.

Similar data to study the downstream evolution of the vortex were acquired at the same station within the tunnel, as discussed earlier, but shifting the fin to locations closer to the laser sheet. These data are found in Beresh et al. (2009a) but not repeated here, except in limited form as part of the subsequent analysis.

Four sample instantaneous vector plots are given in Fig. 4 for $\alpha = 10°$ and $x/c = 4.18$. The vortex structure is observed to be essentially the same as the mean, though exhibiting clear characteristics of instability and turbulence, even while the spatial positioning varies temporally. The mean vortex center as determined from Fig. 3 is $z/c = 0.15$ and $y/c = 0.49$, but the individual realizations of Fig. 4 have centers whose positions vary by as much as $0.05c$ from the mean. This is not dramatic motion but could be sufficient to cause the vortex core appear to have a larger diameter and a reduced peak tangential velocity while creating apparent turbulent stresses (Baker et al. 1974; Devenport et al. 1996; Heyes et al. 2004; Bailey et al. 2006; Bailey and Tavoularis 2008; Westphal and Mehta 1989).

Additional differences can be seen in the instantaneous data of Fig. 4 when compared to the mean of Fig. 3. The most obvious contrast lies in the turbulent fluctuations well outside the vortex core, for both the in-plane velocities and the streamwise component. Patches of turbulence are evident spiraling in toward the vortex core, particularly when examining the streamwise velocity deficit, as the vortical motion rolls up the fin wake shear layer and additionally lifts fluid from the turbulent wall boundary layer. The magnitude of the axial velocity deficit also is seen to vary considerably from the mean value. Another striking feature of Fig. 4 is that the vortex core is not necessarily circular in

Fig. 4 Sample instantaneous realizations of the velocity field at $\alpha = 10°$ and $x/c = 4.18$
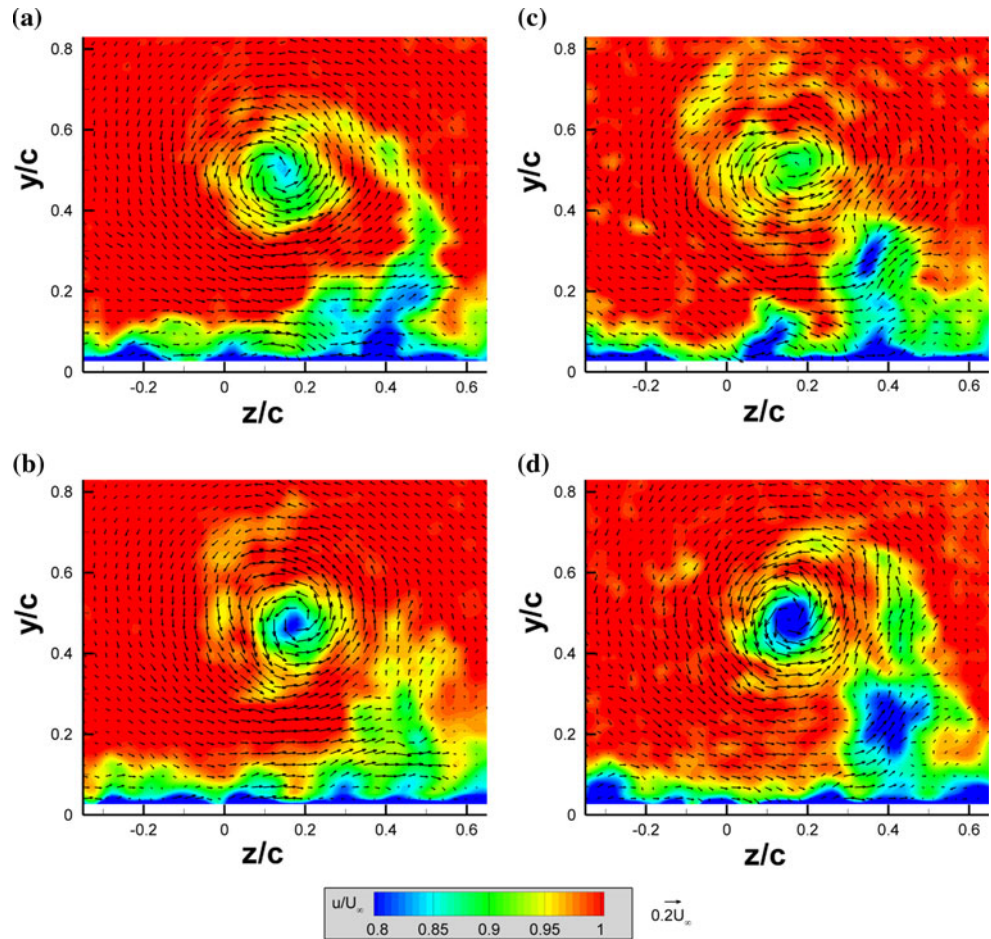
an instantaneous sense; this is most evident in Fig. 4c. This suggests that the turbulence penetrates the boundary of the vortex core, with implications that will be discussed in detail subsequently.

3.2 Instantaneous vortex position

The instantaneous position of the vortex center can be obtained from each individual PIV velocity field by first computing the swirling strength (defined as in Zhou et al. 1999), which offers an advantage over finding the vorticity field in that swirl is sensitive only to rotation and not to shear such as that from the wall boundary layer. (However, for the present purposes, it was found that the peak vorticity and peak swirl nearly always coincided since shear effects are sufficiently distant from the vortex core.) Once the swirl field was calculated, a precise vortex location was found by fitting a three-point Gaussian estimator in the vicinity of the peak of the swirl field independently on the z and y axes, analogous to the peak-fitting commonly used in PIV processing software. The coordinates for the vortex centers identified for each vector field in the $\alpha = 10°$, $x/c = 4.18$ case (2,400 in all)
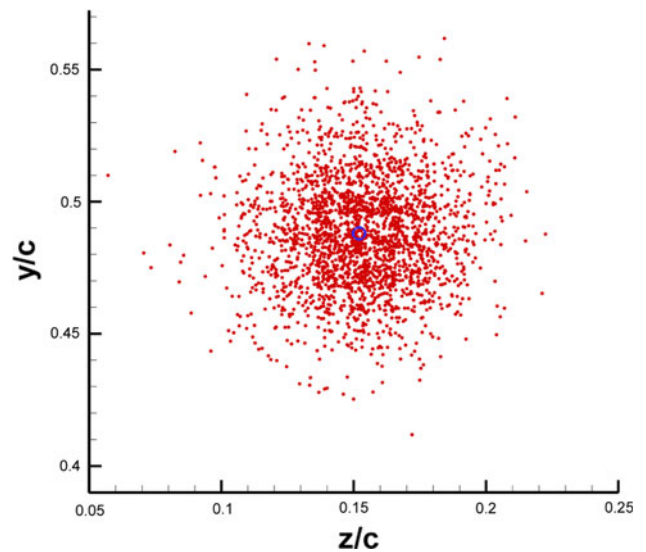

Fig. 5 Instantaneous positions of the vortex center due to vortex meander, for $\alpha = 10°$ and $x/c = 4.18$. The *blue circle* provides the mean position

are plotted in Fig. 5. (Note that the axis scales in Fig. 5 differ from those in Figs. 3, 4.) The uncertainty for this process is estimated as $\pm 0.003c$.

The magnitude of the vortex meandering can be characterized by finding the standard deviation of the instantaneous vortex centers, but this approach had considerable noise. An improved process can be implemented by assuming that the meander follows a Gaussian distribution. Devenport et al. (1996) made the same assumption and Heyes et al. (2004) subsequently confirmed it, with additional support from Bailey and Tavoularis (2008). Presently, a histogram was constructed of the vortex positions, independently for each axis, and then a Gaussian distribution was fit to it and the standard deviation was extracted as one of the fitting parameters.

Figure 6 shows the fitted Gaussian profiles and the histogram points upon which they are based for different fin angles of attack and different stations downstream of the fin trailing edge. Results were omitted for the $\alpha = 2°$ vortex found in Beresh et al. (2009a)m, because its low strength made it too difficult to accurately locate the vortex center. Figure 6a shows that the width of the Gaussian profiles, and hence the meander amplitude, increases distinctly for smaller fin angle of attack. Results are given independently for each axis but show no significant difference. The profile width also increases in Fig. 6b as downstream distance increases, though this effect is much

smaller and requires close scrutiny to distinguish. Some difference between the two axes appears to arise nearer the fin trailing edge. Though not shown, meander measured in the range of Mach 0.5–0.8 shows no Mach dependence, consistent with the mean vortex measurements of Beresh et al. (2009a).

The meander amplitude can be extracted from the Gaussian fits as the standard deviation of the vortex position, again independent on each axis. This reduces the profiles of Fig. 6 to single values that are more easily interpreted. Figure 7 plots these results, σ_z and σ_y, against both the fin angle of attack and the downstream station. The data of Fig. 7a show that an increasing fin angle of attack produces a lower meander amplitude, consistent with previous observations (Devenport et al. 1996; Heyes et al. 2004; Bailey and Tavoularis 2008). The increase in meander amplitude with downstream distance in Fig. 7b also agrees with earlier experiments (Devenport et al. 1996; Jacquin et al. 2001; Heyes et al. 2004; Bailey and Tavoularis 2008). However, Fig. 7b displays another striking feature, namely, that the trend in the meander amplitude suggests a significant non-zero meander at the fin trailing edge. This stands in direct contrast to the previous meander experiments showing a trend likely to produce zero

Fig. 6 Probability density functions of the vortex meander distances where *solid lines* and *filled circles* show meander on the *z* axis and *broken lines* and *hollow triangles* show meander on the *y* axis; **a** varying α at constant $x/c = 4.18$; **b** varying x/c at constant $\alpha = 10°$
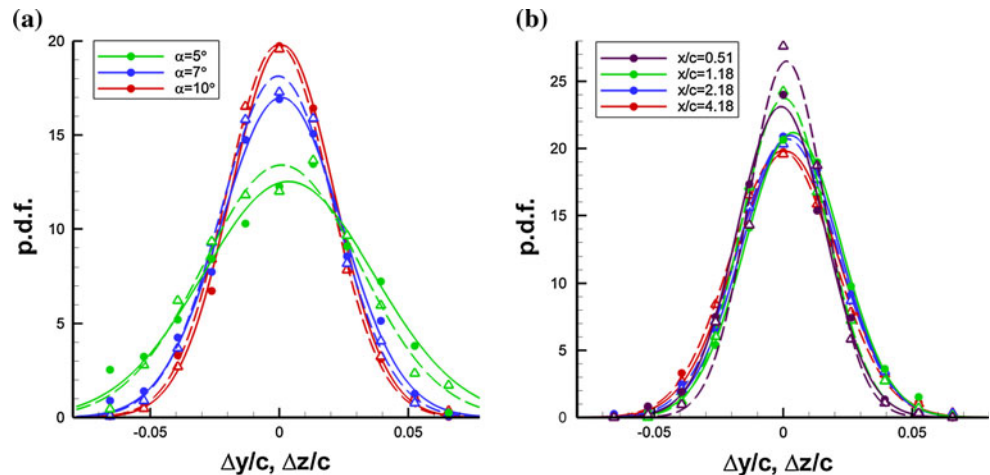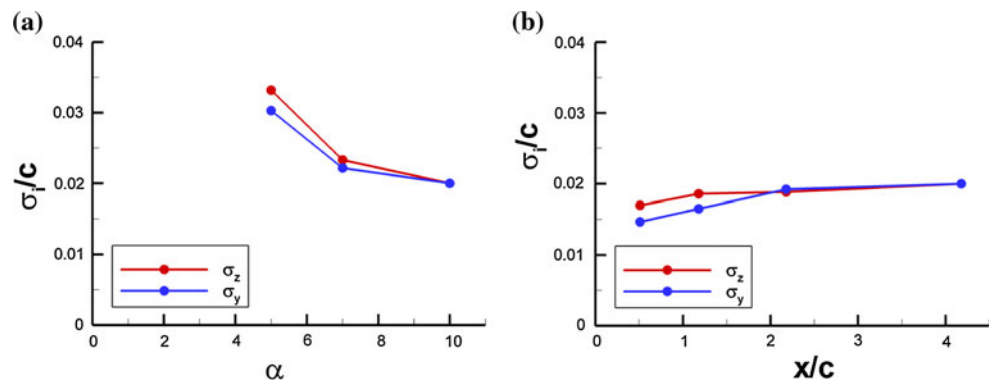

Fig. 7 Vortex meander amplitude, computed independently for each axis; **a** varying α at constant $x/c = 4.18$; **b** varying x/c at constant $\alpha = 10°$

meander (or nearly so) at the lifting surface trailing edge (Devenport et al. 1996; Heyes et al. 2004; Bailey and Tavoularis 2008). This implies that the present vortex begins to meander even as it develops on the surface of the fin.

In the present case, the typical vortex core meander distance at a downstream position of $x/c = 4.18$ is about $0.02c$ with no discernable preferential direction, and a maximum meander distance of about $0.05c$. Though reported meander distances vary greatly, these results appear approximately consistent with other investigations (Green and Acosta 1991; Devenport et al. 1996; Heyes et al. 2004; Yeung and Lee 1999), excepting Corsiglia et al. (1973) who display motion nearly two orders of magnitude higher. Some studies find no significant meander at all (Chow et al. 1997; Gerontakos and Lee 2006).

From Fig. 7a as well as Devenport et al. (1996) and Heyes et al. (2004), it is evident that as the vortex becomes stronger, it is more resistant to vortex meander. This suggests that meander is caused by an external source whose influence is lessened as it remains constant while the vortex strength increases, as opposed to a self-induced source whose influence would be expected to rise in concert with the vortex strength. It is not possible to state based solely upon Fig. 7a whether this external influence is freestream turbulence, as widely believed, or a response to turbulence within the boundary layer shed from the lifting surface or, in the present case, the boundary layer upon the wind tunnel wall. Though a stronger vortex would lift more of the wall boundary layer toward the vortex core, the turbulent fluctuation magnitude in the boundary layer would not rise with vortex strength, nor is it yet clear to what extent these fluctuations penetrate the core, so again it is not possible to identify the source of the vortex meandering from the data shown thus far.

3.3 Effects of meander

As noted earlier, vortex meander has been observed to create artificially reduced tangential and axial velocities and an enlarged core radius (Devenport et al. 1996; Heyes et al. 2004; Bailey and Tavoularis 2008); Devenport et al. (1996) and Bailey and Tavoularis (2008) each devised methods of correcting their hot-wire anemometry data for vortex meander to produce the velocity profiles that would result in the absence of meander. The Devenport approach assumed non-isotropic Gaussian meander and a fitted velocity profile, from which the meander's contribution to mean and turbulent properties could be removed once the standard deviations and correlation coefficients of the meander distance were determined from the hot-wire signal. Bailey and Tavoularis (2008) took an approach requiring fewer assumptions about the nature of the vortex behavior, based upon the zero-crossing frequency of the vortex center as it passes the probe; results were found to be in reasonable agreement with Devenport's technique. Heyes et al. (2004) confirmed the Devenport approach using their full-field PIV data by relocating the vortex center of each instantaneous velocity field.

A correction for vortex meander similar to Heyes et al. (2004) was conducted using the present data set. The instantaneous vortex position is known from the peak of the swirling strength field, from which each vector field may be re-centered to the mean vortex position. Vectors are interpolated onto a common grid; then, an average is taken over all the repositioned velocity fields to provide corrected values for the peak tangential velocity, vortex radius, and other mean properties. Because the entire vortex is visualized at each instant, unlike the time-sequenced point measurements of hot-wire anemometry, no assumptions are required regarding the nature of the vortex meander.

Figure 8 displays profiles through the mean vortex center of both the tangential velocity and the axial velocity, using both the original data and the re-centered data, for the case in which $\alpha = 10°$ and $x/c = 4.18$. The corrections due to re-centering are found to be insignificant. Devenport et al. (1996), conversely, find that the velocities and radii are altered by 10–15%; Heyes et al. (2004) find mildly smaller effects, and Bailey and Tavoularis (2008) find velocity differences nearing 50% for high levels of

Fig. 8 Velocity profiles through the mean vortex center for the original data and data corrected for meander by re-centering; $\alpha = 10°$ and $x/c = 4.18$; **a** tangential component; **b** axial component
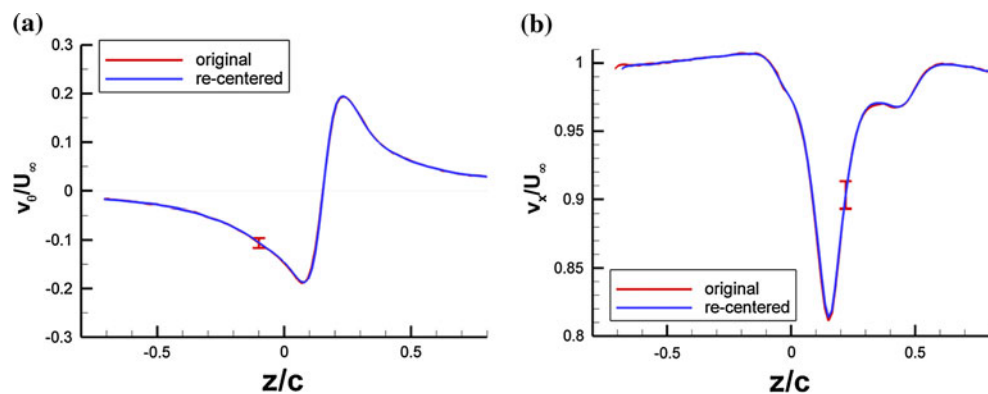
freestream turbulence. However, the first two of these prior experiments examined laminar vortices and the third probably did as well. In the present case, a much greater degree of turbulence appears to be present in the vortex, as suggested by the instantaneous snapshots shown in Fig. 4 and the apparent initiation of vortex meander on the fin surface (Fig. 7b), as well as additional analysis offered subsequently. The insignificance of the meander corrections to the mean velocity profiles in Fig. 8 probably is because turbulent fluctuations in the vortex shape and strength dominate over variations in its position. The same result appears to have occurred in Shah et al.'s (1999) turbulent delta-wing trailing vortex.

The effects of meander upon the turbulence properties, however, are far more profound. The best means of characterizing the turbulence of the vortex is to derive the turbulent kinetic energy k from the velocity data, which is given in Fig. 9a for the $\alpha = 10°$, $x/c = 4.18$ case. The magnitude of k is seen to rise to a maximum concisely located at the center of the vortex core, with elevated levels of turbulence continuing around the vortex core periphery. For reference, the vortex core radius is about $0.08c$; therefore, k can be seen to be about half of its peak at this boundary. Similar levels of turbulence are found in the wind tunnel wall boundary layer and in the portion of it lifted off the wall and pulled toward the vortex, creating the appearance of turbulence drawn from the wall boundary layer into the vortex core where it leads to decay of the vortex.

The picture changes considerably when instead the re-centered data are used to compute the turbulent kinetic energy, shown in Fig. 9b. Now the high levels of turbulence in the center of the vortex core have almost entirely disappeared, with a small but significant degree of turbulence still evident around the vortex core periphery.

Turbulence levels associated with the lifted boundary layer are largely unaffected. This demonstrates that most of the turbulence in the vortex core is an artifact of meander, with a small degree of turbulence shown to be real even in the meandering reference frame. The remaining turbulence around the core appears to originate in the wind tunnel wall boundary layer, as had been suggested by the mean velocity fields of Fig. 3, then rise toward the vortex and penetrate the edge of the core. This hints that the boundary layer turbulence may play a role in the meander of the vortex. The existence of a laminar core at the very center of a trailing vortex while surrounded by turbulence evident near the core radius previously has been observed experimentally (Devenport et al. 1996; Bandyopadhyay et al. 1991) and computationally (Ragab and Sreedhar 1995) and further is supported by analytical studies (Cotel and Breidenthal 1999; Jacquin and Pantano 2002). Such behavior occurs when turbulent fluid crosses the periphery of the vortex and then is relaminarized by the stabilizing effects of the strong rotational motion of the vortex core, reducing the turbulence levels nearer the center of the vortex.

The estimated uncertainty in k due to error in correctly locating the vortex center is ± 0.001, determined by artificially generating turbulence by randomly re-centering the mean velocity field according to the expected uncertainty in finding the vortex center. Additionally, it must be noted that even after correction for vortex meander, the turbulent kinetic energy fields are, strictly speaking, not solely a measure of true turbulence because they also are subject to instabilities leading to vortex decay. In addition to the familiar turbulent eddies, velocity fluctuations may originate from geometric distortions of the vortex (such as observed in Fig. 4c) and variations in the axial velocity (compare the four snapshots of Fig. 4), both phenomena known to precede the turbulent breakdown of a vortex.

Fig. 9 Turbulent kinetic energy fields for $\alpha = 10°$, $x/c = 4.18$. a raw data; b re-centered data

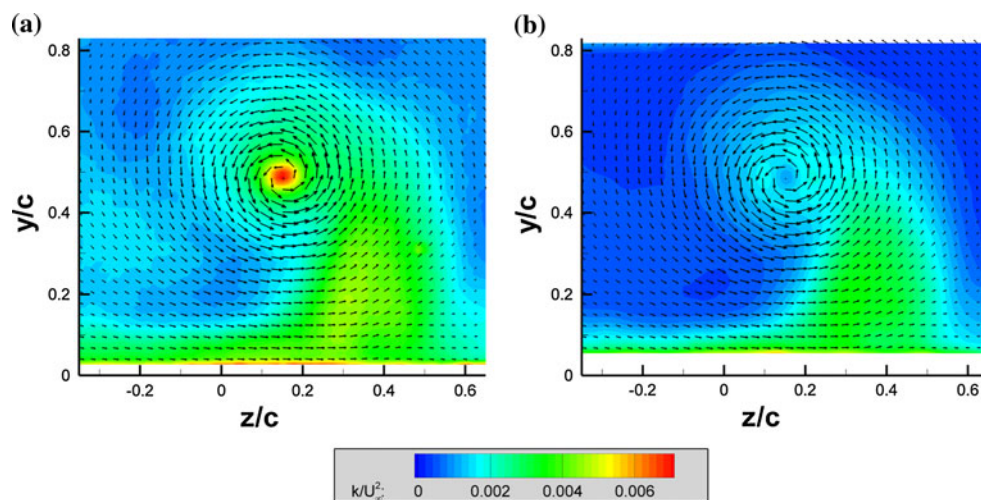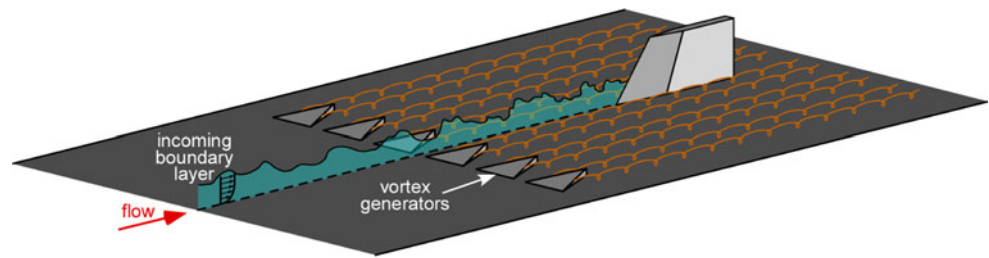## 3.4 Energized boundary layer

To establish whether the turbulence within the wind tunnel wall boundary layer is a direct influence upon the vortex meander, an additional experiment was conducted in which the incoming wall boundary layer was energized through the use of low-profile vortex generators placed upstream of the fin. The benefits of vortex generators (VG's) previously have been recognized in reducing flow separation, shock wave strength, and other aspects of passive flow control (Lin 2002; Ashill et al. 2005). They function by shedding vortices from their trailing edge(s) to churn up the boundary layer and raise the most turbulent fluid near the wall into the outer layer, while maintaining a low-profile geometry that keeps the VG's themselves submerged within the boundary layer to limit any drag penalty. Smith (1994) provides an analysis of wedge-shaped VG's that offers guidance on the selection of geometric parameters for maximum effectiveness, which, coupled with Lin (2002) and Ashill et al. (2005), suggest that the wedges shown in Fig. 10 would be most appropriate to the current purpose. They are 0.35 δ (5.6 mm) in height, 1.6 δ (25 mm) wide, and 2.0 δ (31 mm) long. Six were placed a short distance upstream of the fin root leading edge, spaced by 2.1 δ (32 mm) centerline to centerline.

The resulting mean velocity field of the trailing vortex within the energized incoming boundary layer is given in Fig. 11, which is the complement of the undisturbed case in Fig. 3. The vortex itself appears largely the same, though the axial velocity deficit in the vortex core is lessened and a close inspection reveals a decrease in the tangential velocity component, both indicative of the impact of greater vortex meander on the mean vortex, or perhaps, accelerated vortex decay. The streamwise velocity deficit associated with the wall boundary layer lifted from the surface can be seen to cover a significantly greater spatial extent, suggesting that more boundary layer turbulence is drawn inward toward the vortex core. The meander of the vortex may be examined directly in the same manner as previously described and is shown in Fig. 12, the equivalent of Fig. 6. Here, curves are shown for the energized boundary layer case and the earlier undisturbed case, from which it is readily evident that the meander distance has increased markedly with the presence of the VG's. The
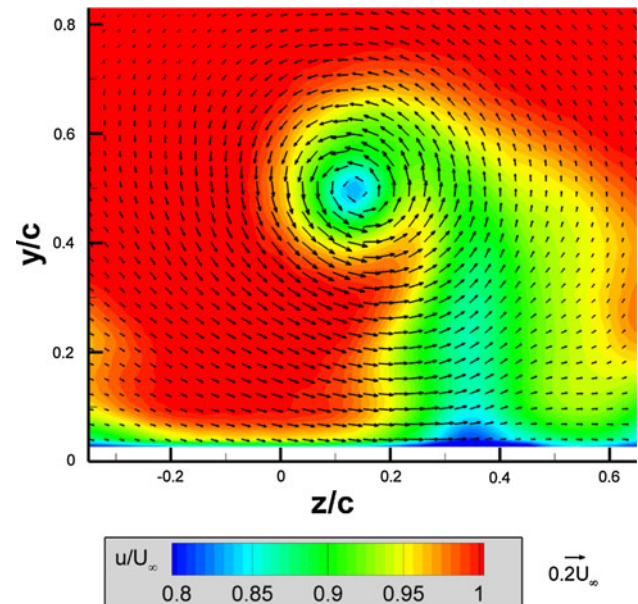

Fig. 11 Mean velocity field at $\alpha = 10°$ and $x/c = 4.18$ in the energized boundary layer
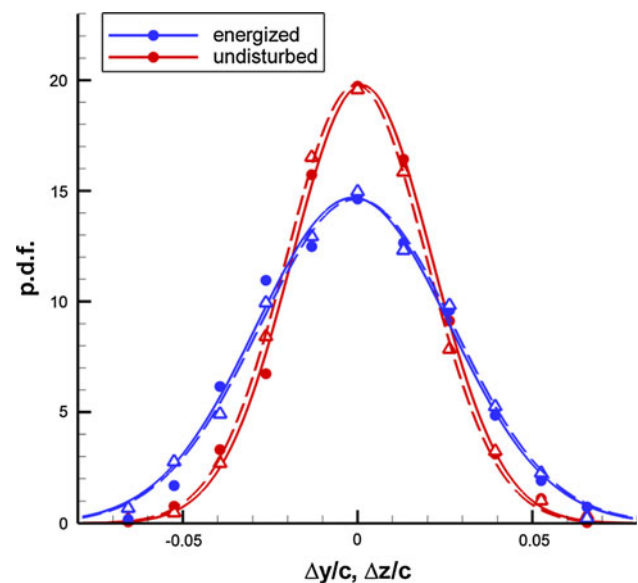

Fig. 12 Probability density functions of the vortex meander distances for the energized and undisturbed boundary layer cases; *solid lines/ filled circles* for the z axis and *broken lines/hollow triangles* for the y axis
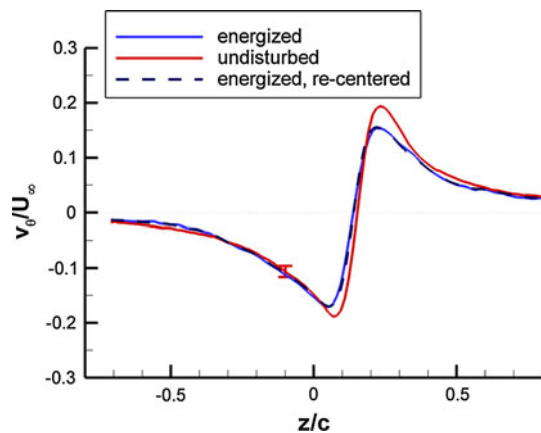
Fig. 13 Mean tangential velocity profiles at $\alpha = 10°$ and $x/c = 4.18$ in the energized boundary layer

Fig. 14 Turbulent kinetic energy field for $\alpha = 10°$ and $x/c = 4.18$ in the energized boundary layer, corrected for meander by re-centering the data

standard deviations of the vortex position extracted from the energized boundary layer case are $\sigma_z = \sigma_y = 0.028c$, compared with $\sigma_z = \sigma_y = 0.020c$ for the undisturbed case, showing a substantial increase in the meander magnitude. These results clearly demonstrate that the energized boundary layer does increase the vortex meander and hence the wind tunnel wall boundary layer is indeed a factor in this phenomenon.

The effects of the increased meander may be examined for the energized boundary layer in comparison to the earlier undisturbed case. An extracted mean velocity profile through the vortex center is displayed in Fig. 13 along with the undisturbed profile from Fig. 8a. Two profiles are shown for the energized boundary layer case, one determined from the raw data and a second from data re-centered on the instantaneous position of the vortex core to remove the effects of meander. As in the undisturbed case, no significant difference is found when the data are re-centered, indicating that, as before, turbulent fluctuations dominate over positional variation. However, the peak magnitudes of the tangential velocity are clearly lessened for the energized boundary layer, a result of the increased turbulence causing the vortex to decay faster and therefore display a lower tangential velocity. The vortex core radius can be calculated from the velocity fields as well, which show an increase from a value of $0.079c$ for the undisturbed boundary layer case to $0.087c$ for the energized boundary layer; this too is representative of a more rapid vortex decay.

Figure 14 shows the turbulent kinetic energy fields for the energized boundary layer case, derived from the re-centered data to accurately represent the turbulence near the vortex core. As for the undisturbed boundary layer in Fig. 9, the artificial turbulence at the vortex center is absent in the re-centered data and the turbulence levels found in the wall boundary layer are comparable in the two cases.
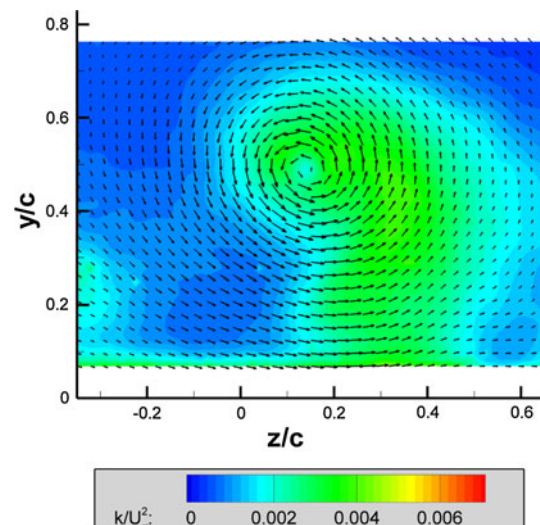
However, for the energized boundary layer, the expanse of turbulence lifted from the wall toward the vortex is noticeably larger, and the annulus of turbulence approximately coincident with the periphery of the vortex core is both thicker and stronger (the peak value of k/U_∞ in the vortex core is about 0.0035 for the energized boundary layer case compared to about 0.0018 for the undisturbed case). This indicates that more turbulent fluid is found penetrating the vortex core in the presence of the energized boundary layer—though some relaminarization still occurs—and that a greater turbulent influence upon the flow can be anticipated. And in fact, that is what occurs: greater vortex meander is observed, reduced tangential velocities are measured, and the vortex core radius increases. These phenomena all are consistent with an enhanced turbulent influence upon the vortex.

4 Discussion

The experiment conducted in the energized boundary layer has established that turbulence within the wind tunnel wall boundary layer is in fact a source of the meander of the fin trailing vortex, but it does not suggest that the usual sources (freestream turbulence, shear layer instabilities, etc.) are not present as well, nor does it imply that boundary layer turbulence is the dominant effect. Neither does the experiment provide a mechanism by which the boundary layer turbulence reaches the vortex. The most obvious explanation is that the vortical rotation lifts the wall boundary layer and draws it into the vortex core, as suggested by the mean velocity field of Fig. 3. Unfortunately, this interpretation suffers at least two deficiencies.

First, it would imply that meander does not begin until after the vortex has been shed from the fin and rolls up, which contradicts the observation in Fig. 7b that meander appears to initiate upon the fin surface prior to shedding of the vortex. Secondly, no wall boundary layer fluid can plausibly reach the vortex until it is several chord lengths downstream of the fin trailing edge. This conclusion arises from estimating the length of time required for fluid to travel from the wall boundary layer to the vortex core; at the observed tangential velocities and a spiral path length of approximately one chord length c, about 1–2 ms would be necessary. In this time, the vortex would convect about 3–7 chords from the fin trailing edge at the freestream velocity. Meander, of course, begins well before this arrival time so some other means must exist by which the wind tunnel wall boundary layer influences the vortex meander.

Some of the turbulence seen spiraling in toward the vortex core actually originates in the shear layer behind the fin. This best can be seen by examining the turbulent kinetic energy fields at stations nearer the fin trailing edge, as given in Fig. 15, in which the data have been re-centered to correct for vortex meander. Considerably elevated turbulence can be seen in both the wake shear layer and the trailing vortex as they are shed from the fin, which then diminish substantially as they travel downstream. These data also show that the boundary layer fluid drawn from the wall actually originates in a corner vortex formed in the junction between the leeside of the fin and the wind tunnel wall that then propagates downstream, though the presence of this additional structure does not preclude fluid from the boundary layer eventually entering the spiral wake; the formation of this corner vortex may be seen in greater detail in Beresh et al. (2009b). Nonetheless, despite the greater complexity of the flowfield than previously apparent, the experiment conducted in the energized boundary layer demonstrates that turbulence from the incoming boundary layer still plays a role in the meander and decay of the vortex.

An alternative explanation may be assembled by considering the formation of the vortex on the surface of the fin. For a low-aspect-ratio lifting surface with a swept leading edge, such as the present fin, a vortex is known to form along this edge and then subsequently moves to the fin tip before it is shed at the trailing edge (Lamar 1998). Beresh et al. (2009b) confirmed this behavior for the present fin geometry using PIV measurements on the fin surface and additionally showed that the vortex remains stable despite predictions of vortex breakdown on the fin surface (Breitsamter 2008). Lift coefficient curves (Smith et al. 2009) show no evidence of vortex breakdown either. The discrepancy probably is due to the small size of the current fin, as independent studies have shown that at low values of the Reynolds number, the location of vortex breakdown is delayed (Taylor and Gursul 2004; Elkhoury and Rockwell 2004). Regardless, the trailing vortex initiates its development at the apex of the fin, which places it within the incoming wind tunnel wall boundary layer when it first forms. At this early stage in the vortex's lifetime, it already is exposed to the boundary layer turbulence, raising the possibility that an instability is introduced to the incipient vortex core even as it originates and thus providing a mechanism for the influence of the boundary layer compatible with the present experimental observations.

Some precedent for this hypothesis may be found from delta-wing experiments. Studies have shown unsteady vortex motion can occur on the surface of a delta wing even prior to vortex breakdown (Menke and Gursul 1997; Gordnier and Visbal 2005), which Gursul and Xie (2000) attribute to a Kelvin–Helmholtz instability in the shear layer over the swept leading edge. This instability may be present in the current experiment, but it is insufficient to explain the increased meander due to the energized boundary layer while the fin geometry remains unaltered. Nonetheless, these delta-wing investigations show that the developing vortex is susceptible to meandering due to a perturbation near its origin, which in the present case is likely to be the wind tunnel wall boundary layer turbulence.

Finally, it is necessary to note that the vortex meander is not, in part or in whole, attributable to vibration of the fin,

Fig. 15 Turbulent kinetic energy fields for $\alpha = 10°$, at multiple downstream stations in the undisturbed boundary layer, corrected for meander by re-centering the data

x/c=0.51

x/c=1.18

x/c=2.18

x/c=4.18

k/U_∞^2: 0   0.002   0.004   0.006
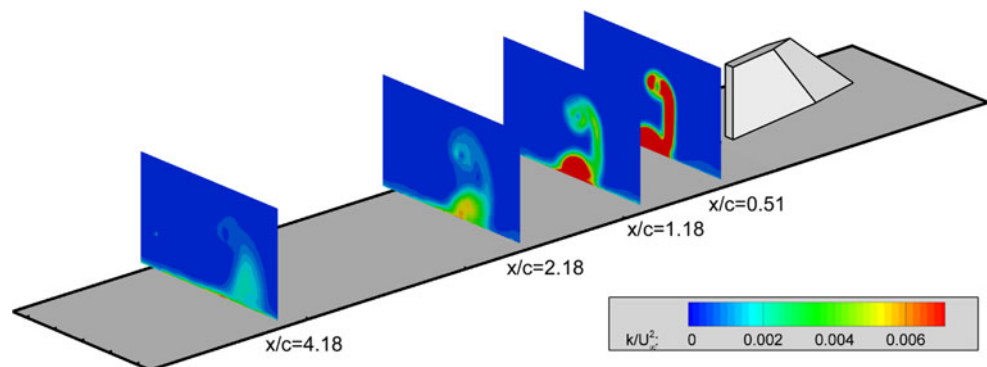
as photographic observation of the fin trailing edge showed no discernable motion.

The current results imply that vortex meander may be a phenomenon present in flight for missile geometries, not merely isolated to wind tunnel studies as supposed in past meander experiments, because the vortices produced by missile fins would entrain any turbulence found in the boundary layer growing on the missile body itself, analogous to the test section wall boundary layer in the present work. This influence of the nearby wall on vortex meander differs for a trailing vortex shed from a low-aspect-ratio fin as opposed to a vortex shed from an aircraft wing whose tip is much further distant from a wall. Vortex meander in flight may have implications for buffeting and vibrational loading, especially on guided-missile configurations that possess multiple sets of control surfaces in which vortices shed from upstream canards or strakes would impinge upon downstream fins.

5 Conclusion

A sub-scale experiment has been conducted to study the trailing vortex shed from a tapered fin installed on a wind tunnel wall to represent missile configurations. Measurements have been acquired using stereoscopic particle image velocimetry in the crossplane to understand the low-frequency meander of the vortex. Data were acquired at several different downstream locations behind the trailing edge of the fin but still within the near-field of the flow, for multiple fin angles of attack at Mach 0.8. The full-field velocity measurements allow a direct examination of the instantaneous position of the vortex, in contrast to the data possible using time-sequenced point measurements as in most previous vortex meander studies. Distributions of the instantaneous vortex positions, which are found from each individual velocity field, show that the meander amplitude increases with downstream distance and decreases with vortex strength, consistent with previous studies to indicate that the meander is induced by an influence external to the vortex itself. Trends with downstream distance suggest that meander begins on the surface of the fin itself, prior to vortex shedding.

Individual velocity fields reveal a vortex possessing turbulent characteristics. In addition to the meander in spatial position, patches of turbulence are observed spiraling toward the vortex core, the magnitude of the axial velocity deficit varies significantly, and the vortex structure may distort from the ideal circular shape. Smoothing effects previously have been observed upon the mean properties of the vortex due to meander, which have been corrected by re-centering each individual vector field on its instantaneous vortex center, and then recalculating the mean and turbulent properties. No significant changes in the mean velocities are found in the meandering reference frame, which appears to be because turbulent fluctuations in the vortex shape and strength dominate over variations in its position. Conversely, the turbulent kinetic energy field is dramatically affected. The uncorrected data show a large peak of artificial turbulence at the center of the vortex core, which almost entirely disappears when the data first are re-centered. However, some turbulence remains evident near the core radius even in the meandering reference frame. Measurement planes nearer the fin trailing edge show that this turbulence originates in the fin wake shear layer with additional turbulent fluid drawn from the wind tunnel wall boundary layer. Some of this turbulence appears to penetrate the vortex core but is laminarized near its center by the rotational motion.

The suggestion that turbulence originating at the wind tunnel wall may contribute to the vortex meander was confirmed by energizing the incoming boundary layer using low-profile vortex generators and observing a substantial increase in the meander amplitude. Accordingly, the vortex displays increased effects due to turbulence, where the mean tangential velocities diminish and the vortex core radius expands compared to the undisturbed boundary layer. A greater degree of turbulent kinetic energy is found to penetrate the vortex core, even when corrected for meander. Though wall boundary layer turbulence clearly is a source of vortex meander, other known contributors such as freestream turbulence likely remain present and no conclusions may be drawn regarding their relative influence.

A mechanism for the influence of the incoming boundary layer on the vortex meander has been hypothesized, in which the vortex initially forms at the apex of the swept leading edge of the fin, submerged within the wind tunnel wall boundary layer where it is exposed to turbulent fluctuations. Thus, an instability is introduced into the incipient vortex core even as it develops, leading to meander on the fin surface and the turbulent properties observed in the trailing vortex. These results demonstrate that for low-aspect-ratio lifting surfaces in proximity to a wall, such as missile fins, vortex meander results from the wall boundary layer turbulence as well as known sources such as turbulence from the wind tunnel freestream or the lifting surface wake. Such observations also imply that meander may be present in flight as well owing to the turbulent boundary layer that grows on the missile body surface.

References

Ashill PR, Fulker JL, Hackett KC (2005) A review of recent developments in flow control. Aeronaut J 109(1095):205–232

Bailey SCC, Tavoularis S (2008) Measurements of the velocity field of a wing-tip vortex, wandering in grid turbulence. J Fluid Mech 601:281–315

Bailey SCC, Tavoularis S, Lee BHK (2006) Effects of freestream turbulence on wing-tip vortex formulation and near field. J Aircraft 43(5):1282–1291

Baker GR, Barker SJ, Bofah KK, Saffman PG (1974) Laser anemometer measurements of trailing vortices in water. J Fluid Mech 65(2):325–336

Bandyopadhyay PR, Stead DJ, Ash RL (1991) Organized nature of a turbulent trailing vortex. AIAA J 29(10):1627–1633

Beresh SJ, Henfling JF, Erven RJ, Spillers RW (2005) Penetration of a transverse supersonic jet into a subsonic compressible crossflow. AIAA J 43(2):379–389

Beresh SJ, Henfling JF, Spillers RW (2009a) Planar velocimetry of a fin trailing vortex in subsonic compressible flow. AIAA J 47(7):1730–1740

Beresh SJ, Henfling JF, Spillers RW (2009b) Formation of a fin trailing vortex in undisturbed and interacting flows. AIAA Paper 2009-3892

Breitsamter C (2008) Unsteady flow phenomena associated with leading-edge vortices. Prog Aerosp Sci 44(1):48–65

Chow JS, Zilliac GG, Bradshaw P (1997) Mean and turbulence measurements in the near field of a wingtip vortex. AIAA J 35(10):1561–1567

Corsiglia VR, Schwind RG, Chigier NA (1973) Rapid scanning, three-dimensional hot-wire anemometer surveys of wing-tip vortices. J Aircr 10(12):752–757

Cotel AJ, Breidenthal RE (1999) Turbulence inside a vortex. Phys Fluids 11(10):3026–3029

Devenport WJ, Rife MC, Liapis SI, Follin GJ (1996) The structure and development of a wing-tip vortex. J Fluid Mech 312:67–106

Elkhoury M, Rockwell D (2004) Visualized vortices on unmanned combat air vehicle planform: effect of Reynolds number. J Aircr 41(5):1244–1247

Gerontakos P, Lee T (2006) Near-field tip vortex behind a swept wing model. Exp Fluids 40(1):141–155

Gordnier RE, Visbal MR (2005) Compact difference scheme applied to simulation of low-sweep delta wing flow. AIAA J 43(8):1744–1752

Green SI, Acosta AJ (1991) Unsteady flow in trailing vortices. J Fluid Mech 227:107–134

Gursul I, Xie W (2000) Origin of vortex wandering over delta wings. J Aircr 37(2):348–350

Heyes AL, Jones RF, Smith DAR (2004) Wandering of wing-tip vortices. Proceedings of the 12th international symposium on applications of laser techniques to fluid mechanics, Lisbon, Portugal, Paper 35-3

Jacquin L, Pantano C (2002) On the persistence of trailing vortices. J Fluid Mech 471:159–168

Jacquin L, Fabre D, Geffroy P, Coustols E (2001) The properties of a transport aircraft wake in the extended near field: an Experimental Study. AIAA Paper 2001-1038

Lamar JE (1998) The use and characteristics of vortical flows near a generating aerodynamic surface: a perspective. Prog Aerosp Sci 34(3–4):167–217

Lin JC (2002) Review of research on low-profile vortex generators to control boundary-layer separation. Prog Aerosp Sci 38(4–5):389–420

Melling A (1997) Tracer particles and seeding for particle image velocimetry. Meas Sci Technol 8(12):1406–1416

Menke M, Gursul I (1997) Unsteady nature of leading edge vortices. Phys Fluids 9(10):2960–2966

Ragab S, Sreedhar M (1995) Numerical simulation of vortices with axial velocity deficits. Phys Fluids 7(3):549–558

Rokhsaz K, Foster SR, Miller LS (2000) Exploratory study of aircraft wake vortex filaments in a water tunnel. J Aircr 37(6):1022–1027

Samimy M, Lele SK (1991) Motion of particles with inertia in a compressible free shear layer. Phys Fluids A 3(8):1915–1923

Shah PN, Atsavapranee P, Hsu TY, Wei T, McHugh J (1999) Turbulent transport in the core of a trailing half-delta-wing vortex. J Fluid Mech 387:151–175

Shekarriz A, Fu TC, Katz J, Huang TT (1993) Near-field behavior of a tip vortex. AIAA J 31(1):112–118

Smith FT (1994) Theoretical prediction and design for vortex generators in turbulent boundary layers. J Fluid Mech 270:91–131

Smith JA, Beresh SJ, Henfling JF, Grasser TW, Spillers RW (2009) Aerodynamic correlations for a fin with a vortex-induced angle of attack. AIAA Paper 2009-1089

Soloff SM, Adrian RJ, Liu ZC (1997) Distortion compensation for generalized stereoscopic particle image velocimetry. Meas Sci Technol 8(12):1441–1454

Taylor GS, Gursul I (2004) Buffeting flows over a low-sweep delta wing. AIAA J 42(9):1737–1745

Westphal RV, Mehta RD (1989) Interaction of an oscillating vortex with a turbulent boundary layer. Exp Fluids 7(6):405–411

Yeung AFK, Lee BHK (1999) Particle image velocimetry study of wing-tip vortices. J Aircr 36(2):482–484

Zhou J, Adrian RJ, Balachandar S, Kendall TM (1999) Mechanisms for generating coherent packets of hairpin vortices in channel flow. J Fluid Mech 387:353–396